ROYAL SOCIETY
OF CHEMISTRY

PAPER

Check for updates

Investigation of MnSc₂X₄ (X = S, Se) spinels to unveil their potential for optoelectronic and thermoelectric applications

Syed Ali Raza,[a] Ghulam M. Mustafa, [ID] *[b] M. Adil Ameer,[b] N. A. Noor, [ID] [c]
Zahid Farooq,[b] Sohail Mumtaz [ID] *[d] and Ihab Mohamed Moussa[e]

To advance the fields of optoelectronics and thermoelectrics, the demand for developing novel materials with exceptional optoelectronic and thermoelectric characteristics has greatly increased. In this respect, spinels are among the well-researched materials in the scientific community. The present study examines the mechanical, optoelectronic, magnetic, and thermoelectric characteristics of MnSc₂X₄ (X = S, Se), utilizing the WIEN2k and BoltzTrap code. The investigated materials exhibit cubic structures with the $Fd\bar{3}m$ space group and lattice parameters of 10.44 and 10.94 Å for S- and Se-based compositions, respectively. Fulfillment of the Born stability criteria attest to the mechanical stability, while negative formation energies validate the thermodynamic stability of the spinels. The spin-polarized electronic band structure (EBS) and the density of states (DOS) reveal the semiconducting nature of the materials with direct bandgap (E_g). In the optical parameters, MnSc₂S₄ and MnSc₂Se₄ show a static dielectric constant of 6.5 and 8.5, respectively. The materials exhibit wide absorption spectra, ranging from visible to ultraviolet (UV) regions, with the highest absorption in the UV region. The spin-dependent volume optimization demonstrates the ferromagnetic (FM) nature of the materials. The presence of Mn ions in the compositions imparts this magnetic nature to them, which is analyzed by its high local magnetic moment. Lastly, the transport characteristics are analyzed against the increasing temperature in the range of 300−800 K. These materials exhibit high Seebeck coefficients of 242 to 251 μV K⁻¹, and their electrical and thermal conductivities increase with temperature. The figure of merit ZT showed an almost constant value at varying temperatures. The outcomes of this study demonstrate the investigated materials as potential candidates for optoelectronic and thermoelectric applications.

1. Introduction

Optoelectronics is a rapidly growing field that relies on the quantum mechanical interaction between light and electronic materials.[1] It is now extensively applied in the fields of energy harvesting,[1] light and display technology,[2] sensors,[3] medical,[4] and communication technology.[5] Recent advances in the field of optoelectronics include the consequences of the discovery of such new materials that exhibit structural and thermal stability, tunable electronic properties, and high quantum and power conversion efficiencies. In this regard, spinels are emerging

materials that not only fulfill the stability criteria[6,7] but also provide promising optoelectronic characteristics.[8,9] The spinel compounds have a general compositional formula of AB₂X₄ and possess a crystal structure similar to that of the MgAl₂O₄ mineral. In their formula unit, the A and B sites are occupied by cations tetrahedrally and octahedrally coordinated with the X anion, respectively. The A-site cation is typically an alkali or alkaline earth metal or transition metal, and the B-site cation is usually a transition metal. Meanwhile, the X-site comprises chalcogenides or halogen.[10]

Spinel compounds generally cover a wide range of electronic bandgaps (E_g) and show diverse optical properties. Furthermore, the spinels provide the flexibility of modifying their bandgap and other electronic and optical properties by means of substitution or doping.[11,12] Owing to these properties, spinels have been explored as a potential candidate for various applications like solar cells,[13] LEDs,[14] electroluminescence, electrophotocatalysis,[15] and laser diodes.[16] In addition to optoelectronic characteristics, spinels are known for their exceptional thermoelectric and transport properties. Many spinel compounds exhibit high electrical and low thermal conductivity

[a]Department of Physics, Riphah International University, Lahore Campus, Pakistan

[b]Department of Physics, Division of Science and Technology, University of Education, Lahore, Punjab 54770, Pakistan. E-mail: dr.ghulam.muhammad@ue.edu.pk

[c]Department of Physics, University of Sargodha, 40100, Sargodha, Pakistan

[d]Department of Chemical and Biological Engineering, Gachon University, 1342 Seongnamdaero, Sujeong-gu, Seongnam-si 13120, Republic of Korea. E-mail: sohail38@gachon.ac.kr

[e]Department of Botany and Microbiology, College of Science, King Saud University, P. O. Box 2455, Riyadh, 11451, Saudi Arabia

with a high Seebeck coefficient, making them desirable for thermoelectric applications.[17]

Among the spinels, the most investigated compositions comprise chalcogenide-based spinel compounds. The chalcogenide-based compositions exhibit mechanical and thermodynamic stability, which are essential parameters for device fabrication. Regarding the stability of chalcogenide spinels, Noor et al. investigated the spinels $HgSm_2X$ (X = S and Se) and reported the negative enthalpy of formation for these materials, which verified their thermodynamic stability. The reported values of elastic constants fulfilled the mechanical stability criteria.[18] In a related investigation, Mustafa et al. revealed mechanical and thermodynamic stability in the HgY_2X_4 (X = S, Se). Furthermore, the materials were found to exhibit a direct electronic bandgap with a magnitude of 1.2 and 0.6 eV for S and Se-based compositions, respectively.[19] In another study on the tuning of the bandgap, Shahid et al. experimentally prepared the samples of $Mg_{1-x}Sr_xAl_2O_4$ (x = 0.1 to 1.0) and $Mg_{1-x-y}Sr_xMn_yAl_2O_4$ (x = 0.1 to 0.7 and y = 0.1), and reported on the effect of Sr^{2+} and Sr^{2+}/Mn^{2+} doping at the A-site. It was found that for Sr^{2+} doping, the compositions revealed bandgap values in the range of 4.7 to 5 eV. However, the co-doping of Mn^{2+} resulted in a decrease in the bandgap, and gave the values in the range of 2.54 to 3.14 eV.[20] In a comprehensive study of the optoelectronic properties of spinels, Tahir et al. investigated $MgSc_2(S/Se)_4$ and reported direct bandgaps of 2.3 eV and 1.7 eV for S-based and Se-based compositions, respectively. The materials revealed high absorption in the visible and UV regions of the spectrum. In the UV regions, the materials have an absorption coefficient on the order of 10^6 cm^{-1}. The materials were also investigated for their thermoelectric characteristics, and the results demonstrated that materials exhibited high Seebeck coefficient in the range of 220 to 235 µV K^{-1}.[21] In a separate study on the thermoelectric properties of chalcogenide spinels, Sameeullah et al. explored the spinel compounds Ln_2MnSe_4 (Ln = Yb, Lu). They reported that on substituting Yb with Lu in the composition, its thermoelectric performance was improved and the figure of merit values increased from 0.18 to 0.79.[22]

Inspired by the above-mentioned studies on the optoelectronic and thermoelectric characteristics of spinels, we computationally simulated the chalcogenide-based spinels $MnSc_2X_4$ (X = S and Se) on DFT-based WIEN2k software and investigated their mechanical, electronic and optical characteristics. Furthermore, the current work also includes the transport and thermoelectric investigations of the materials which were carried out by employing BoltzTrap code. The results of the present study are promising, and are a worthwhile addition to our current understanding of the properties of spinels, demonstrating the potential of the examined materials for the applications of optoelectronics and thermoelectrics.

2. Computational details

In the present investigations, DFT-based WIEN2k software was utilized to explore the mechanical, opto-electronic and magnetic characteristics of $MnSc_2X_4$ (X = S, Se). Self-consistency calculations were executed using the full-potential linearized augmented plane wave (FP-LAPW) approach. PBE-GGA was used to estimate the exchange–correlation potential. However, it is not very efficient in accurately computing the electronic properties. To eliminate its error, the EBS and DOS were calculated by using the mBJ potential because it provides relatively greater accuracy in the measurement of electronic properties.[23] Moreover, the EBS was further computed using HSE06. To determine the most favorable and lowest ground state of the spinel $MnSc_2X_4$, the ferromagnetic (FM) and anti-ferromagnetic (AFM) configurations for $MnSc_2S_4$ and $MnSc_2Se_4$ were examined in detail. In this analysis, the unit cell that we studied in WIEN2k comprises four S/Se atoms in the $MnSc_2X_4$ structure. The ferromagnetic case was studied considering all the atoms with up-spin orientation, resulting in a net magnetic moment. It is worth noting that a high contribution in magnetic moment arises from the Mn atoms, and the other atoms showed almost a negligible contribution in the total magnetic moment of the unit cell. Keeping this in mind, anti-ferromagnetic orientations were only applied to the four Se atoms assigning the two atoms with up-spin orientation and two with down-spin configuration, resulting in a zero net magnetic moment of the unit cell. Zero net magnetization confirms the true anti-ferromagnetic orientations of the Se-atoms. This orientation of spins in the magnetic lattice allowed for an observable contrast in the electronic and magnetic properties of the spinel. By comparing the two energies, we found the ferromagnetic configuration to be in a more negative range, confirming the ferromagnetic stability of our compound.

The FP-LAPW approach treats the unit cell as two distinct sections: the muffin-tin (MT) or non-overlapping atomic spheres and the interstitial region. The solution of the wave-function in the MT region was assumed to be spherically harmonic, whereas for the interstitial region, a plane-wave solution was considered. Some parameters remained constant throughout the computation, which includes the size of the basic set ($R_{MT} \times K_{max}$), where R_{MT} symbolizes the radius of atomic spheres, and K_{max} depicts the plane wave cutoff. The magnitude of $R_{MT} \times K_{max}$ is set at 8. The other parameter is the angular momentum (ℓ_{max}), which is chosen as 10. The Fourier expansion of charge densities G_{max} was selected as 20. For the sake of good convergence, a mesh of $12 \times 12 \times 12$ was selected in the first Brillion zone, and 10^{-2} mRy was chosen as the energy cutoff. Lastly, the transport parameters were computed using semi-classical Boltzmann theory with constant relaxation time ($\tau = 10^{-14}$ s), and the BoltzTrap and ShengBTE code were utilized to execute the transport and thermoelectric calculations.

3. Results and discussions

3.1 Structural properties

The unit cell structure of the $MnSc_2X_4$ (X = S, Se) spinels are presented in Fig. 1. Fig. 1(a) and (b) represent the molecular model, including the ball-stick and polyhedral representation of the investigated materials, in which the Mn, Sc, and S/Se ions
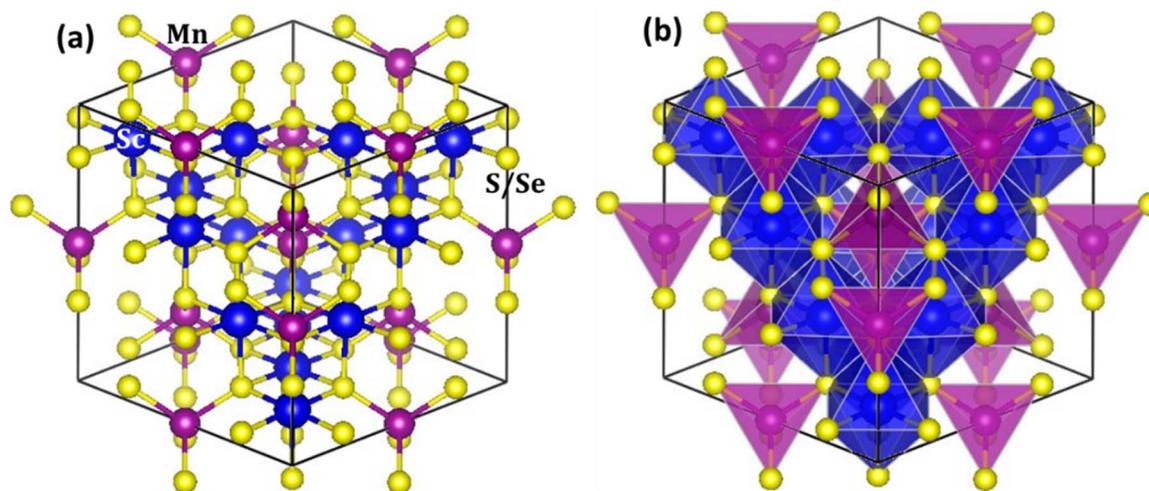
Fig. 1 Unit cell structure of $MnSc_2X_4$ (X = S, Se) (a) ball–stick format and (b) polyhedral model. The Mn, Sc and S/Se ions are displayed with purple, blue and yellow spheres, respectively.

are portrayed by purple, blue and yellow balls, respectively. Furthermore, in Fig. 1, the FCC cubic structure of the unit cells with $Fd\bar{3}m$ space group can be seen, in which Mn has a tetrahedral coordination with S/Se, whereas Sc has an octahedral coordination with S/Se. In the unit cell, the Mn, Sc and S/Se ions have the oxidation states of +2, +3, and −2 and lie at the lattice positions of (0.125, 0.125, 0.125), (0.5, 0, 0) and (0.25, 0.25, 0.25), respectively.[24]

To compute the lattice constants (a_0), the unit cell volume was optimized for the lowest ground state energy. The data obtained from the volume optimization were then fitted in the Birch Murnaghan equation to obtain the smooth curves, which are presented in Fig. 2. From the optimized unit cell volume, we computed the a_0 and listed their magnitudes in Table 1, which are 10.44 Å and 10.94 Å for $MnSc_2S_4$ and $MnSc_2Se_4$, respectively. It can be seen that the lattice constants increase when S in the unit cell is replaced by Se. This is because Se has a comparatively larger ionic radius than S, so when substituted, the unit cell volume rises and the lattice constants subsequently

increase. Furthermore, the volume optimization was utilized to identify the magnetic nature of the spinels. For this purpose, the unit cell volume was optimized sequentially with ferromagnetic (FM) and antiferromagnetic (AFM) spin phases. It can be seen from Fig. 2 that the unit cell with FM spin phase shows lower energy, which shows that the materials are more stable in their FM phase. To probe the thermodynamic stability of the investigated spinels, the formation energies (ΔH_f) of each composition was calculated. The ΔH_f represents the difference of energy between the composition and its constituent ions. In the current instance, it can be written as:

$$\Delta H_f^{MnSc_2S_4} = E_t^{MnSc_2S_4} - E_t^{Mn\text{-}cubic} - 2E_t^{Sc\text{-}hcp} - 3E_t^{S\text{-}orthorhombic} \quad (1)$$

$$\Delta H_f^{MnSc_2Se_4} = E_t^{MnScSe_4} - E_t^{Mn\text{-}cubic} - 2E_t^{Sc\text{-}hcp} - 3E_t^{Se\text{-}trigonal} \quad (2)$$

In the preceding relation, the terms $E_t^{MnSc_2S_4}$ and $E_t^{MnScSe_4}$ depict the total energy of the compound, while $E_t^{Mn\text{-}cubic}$, $E_t^{Sc\text{-}hcp}$, $E_t^{S\text{-}orthorhombic}$ and $E_t^{Se\text{-}trigonal}$ represent the most stable energy values of the constituent elements of Mn, Sc, S and Se,
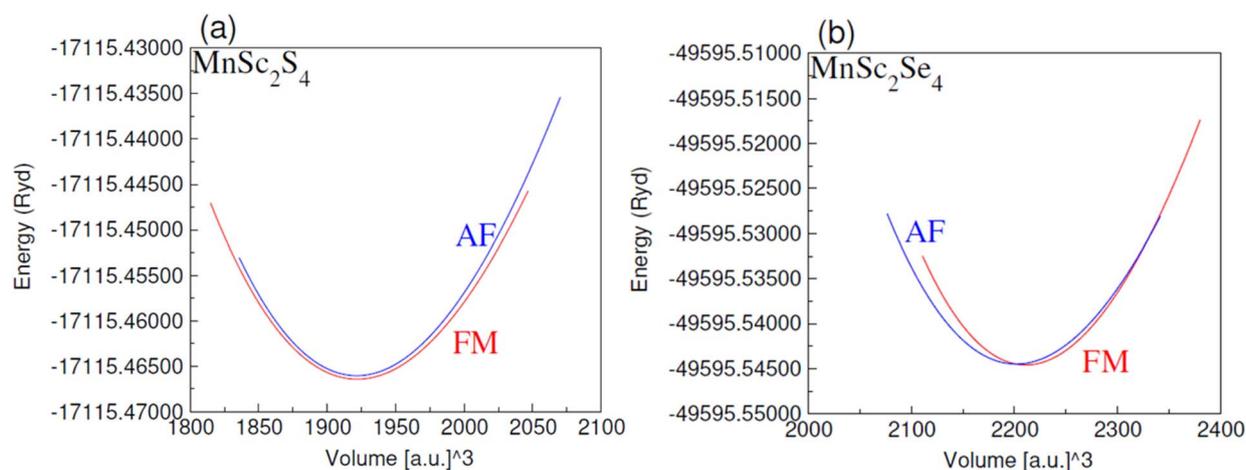

Fig. 2 Computed plots of energy (Ryd) relative to volume ([a.u.]^3) for spinels (a) $MnSc_2S_4$, (b) $MnSc_2Se_4$ in AFM and FM spin-orientations.

Table 1 Optimized magnitudes of a_0 (Å), B_0 (GPa), ΔH_f (eV), and elastic parameters, calculated for $MnSc_2S/Se_4$

Composition	a_0 (Å)	B_0 (GPa)	ΔH_f (eV)	C_{11}	C_{12}	C_{44}	B_0	G	Y	ν	B_0/G
$MnSc_2S_4$	10.44	86.35	−2.86	142.71	51.26	23.16	81.74	30.52	81.42	0.37	2.68
$MnSc_2Se_4$	10.94	71.45	−1.93	135.63	30.76	10.04	65.72	20.92	56.74	0.32	3.14

respectively. Both spinel compositions revealed a negative magnitude of ΔH_f, which shows that their formation involves the exothermic reaction and heat evolves in the formation process. The evolution of heat makes the compounds have less energy than their constituents, which demonstrates their thermodynamic stability. Table 1 tabulates the magnitude of ΔH_f, which is −2.86 and −1.93 eV for $MnSc_2S_4$ and $MnSc_2Se_4$, respectively. From the magnitude of ΔH_f of both compositions, it can be seen that the formation of $MnSc_2S_4$ involves a greater evolution of energy, which means that it is comparatively more thermodynamically stable.

3.2 Mechanical properties

It is highly critical to analyze the mechanical characteristics of the compounds because they directly influence the long-term performance of the fabricated device. To evaluate the mechanical characteristics of $MnSc_2S_4$ and $MnSc_2Se_4$, we computed their elastic stiffness constants, which provide information on the material's behavior to the applied stress. Since the examined spinels exhibit cubic symmetry, the elastic stiffness constants required for the computation are reduced to three: C_{11}, C_{12}, and C_{44}. Furthermore, the mechanical stability of these cubic crystals can be examined by means of the widely known Born stability criteria. As per the criteria, these cubic spinels are considered mechanically stable if they meet the following requirements:[25]

$$C_{44} > 0,\ C_{11} - C_{12} > 0,\ C_{11} + 2C_{12} > 0 \qquad (3)$$

Table 1 tabulates the calculated values of C_{11}, C_{12}, and C_{44}, which satisfy the above-stated necessary conditions for mechanical stability. These elastic stiffness constants (C_{ij}) are very useful in computing the elastic moduli, which incorporate the shear modulus (G), bulk modulus (B_0), and Young's modulus (Y). Through these C_{ij}, we computed the elastic moduli by means of the following relations:[26]

$$B_0 = (C_{11} + 2C_{12})/3 \qquad (4)$$

The magnitude of G is the averaged value of Voigt's and Reuss's shear modulus denoted by G_V and G_R, respectively, and their relations are written below:

$$G_v = (3C_{44} + C_{11} - C_{12})/5\ G_R$$
$$= [5C_{44}(C_{11} - C_{12})]/[4C_{44} + 3(C_{11} - C_{12})] \qquad (5)$$

$$G = (G_R + G_V)/2 \qquad (6)$$

Once the magnitudes of G and B_0 have been measured, then the value of Y can be computed by using the equation given below:

$$Y = (9B_0G)/(3B_0 + G) \qquad (7)$$

Aside from computing B_0 with C_{ij}, the present study also reports the magnitude of B_0 calculated by inserting the data of the optimized volume in the Birch–Murnaghan equation. From the computed values of the elastic moduli, it is apparent that substituting Se in the composition causes a decrease in the elastic moduli, which means that $MnSc_2Se_4$ is less rigid relative to $MnSc_2S_4$. This is due to the relatively lower difference in the electronegativity between Se and the constituent cations. The lower electronegativity difference causes a decrease in the bond strength, which in turn is accountable for the decreases in the elastic moduli.[27] The Pugh's and Poisson's ratios denoted by B_0/G and ν for both materials, respectively, were also calculated. These values provide information on their ductile or brittle nature. A material with $B_0/G > 1.75$ and $\nu > 0.26$ is recognized as ductile; if not, then it is considered as brittle material.[28,29] From the computed magnitude of these ratios, the investigated compositions are considered as ductile materials. Another approach that can be utilized to attest to the ductile nature is Cauchy's pressure, which is computed by $C_{12} - C_{44}$. The ductile materials give a positive magnitude of Cauchy's pressure, whereas the negative Cauchy pressure represents the brittle nature.[30] In the case of the investigated compositions, the positive Cauchy's pressure further validates the ductile character of the two spinels. The computed magnitudes of the elastic moduli and Pugh's and Poisson's ratios are summarized in Table 1.

Many crystal materials are not elastically isotropic and have different magnitudes of elastic parameters in different dimensions. The investigated materials show similar behavior and are anisotropic in nature. Fig. 3 depicts the 3-D illustration of the magnitudes of linear compressibility (β), shear modulus (G), Young's modulus (Y), and Poisson's ratio (ν). It is apparent that except for β, the plots of all the remaining parameters have a non-spherical shape, which reveals that their magnitude varies spatially. Furthermore, we computed the numerical value of anisotropy (A) using the ratio of the maximum-to-minimum magnitudes of the parameters. In the case of $A = 1$, the composition is recognized as isotropic. Meanwhile, in another case, the material is considered anisotropic. The computed values of A reveal the isotropic behavior only for linear compressibility, as seen in Fig. 3. It is noted that the magnitude of A for the Young's and shear moduli increases when Se is substituted in place of S in the composition. However, the anisotropy of Poisson's ratio is relatively greater in $MnSc_2S_4$.

3.3 Electronic properties

Investigations of the electronic characteristics involve an understanding of the electronic conduction mechanism. To this
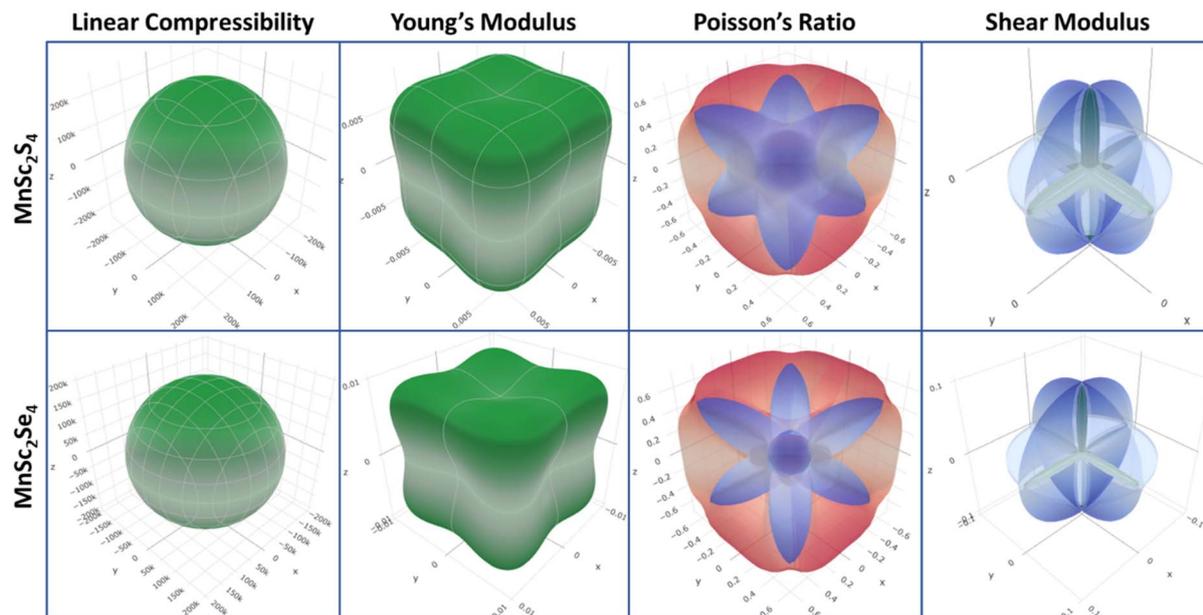
Fig. 3 3-D illustration of the linear compressibility (β), elastic moduli (Y and G) and Poisson's ratio (v) for MnSc$_2$X$_4$ (X = S, Se).

end, we analyzed the electronic conduction mechanism of the investigated materials through their spin-polarized EBS and DOS. The DOS were calculated for energies ranging from -6 eV to $+6$ eV, whereas the EBS was computed from -6 eV to $+6$ eV and -6 eV to $+10$ eV relative to the Fermi level (E_F). Fig. 4(a) and (b) shows the spin-polarized EBS of MnSc$_2$S$_4$ and MnSc$_2$Se$_4$, and the plots in the figure depict different band structures in different spin states computed *via* mBJ potential and HSE-06. The EBS revealed that for both spin channels, E_F occurs between the valence band (VB) and conduction band (CB). This demonstrates the semiconducting nature of the investigated spinels. Moreover, both compositions have a direct bandgap (E_g) because, in both spin configurations, the maxima of VB and minima of CB lie at the same high-symmetry Γ point. In the up-spin configuration, MnSc$_2$S$_4$ and MnSc$_2$Se$_4$ showed a narrow bandgap with the magnitudes of 0.72 and 0.56 eV, respectively. Also, when we employed HSE-06, both compositions revealed semiconducting character with a direct band gap. The calculated bandgaps are 2.2 eV and 1.9 eV for MnSc$_2$S$_4$ and MnSc$_2$Se$_4$, respectively. Conversely, in the down-spin channel, the electronic states of the VB maxima are well below the E_F, which results in an increase in the bandgap. Fig. 4 clearly shows that MnSc$_2$Se$_4$ has a smaller E_g as compared to MnSc$_2$S$_4$. The additional electronic states in Se and its relatively lower electronegativity difference with cations account for this smaller E_g.[31,32] The additional electronic states increase the band size, and the lower electronegativity difference results in its electronic states being less localized. This causes the shifting of electronic bands toward E_F, and consequently leads to the reduction in the bandgap.[33]

The contribution of each ion in the formation of electronic bands was analyzed by plotting the TDOS and PDOS, which correspondingly represent the total and partial density of states.

The Fig. 5(a) and 6(a) show the TDOS while Fig. 5(b–d) and 6(b–d) represent the PDOS plots of MnSc$_2$S$_4$ and MnSc$_2$Se$_4$ respectively. Both figures depict the semiconducting nature in both investigated compositions because the E_F lies between the energy gap. From these figures, it is apparent that in the up-spin configuration, VB of both compositions near the E_F is mainly composed of the 3d–t$_{2g}$ states of Mn. Meanwhile, the contributions from the 3d-states of Sc and 3p/4p-states of S/Se are comparatively small. In the same spin configuration, the CB minima are mainly shaped by the major contribution of the 3d-states of Sc. There is a minor and negligible contribution of the 3p/4p-states of S/Se and 3d-states of Mn, respectively. In the spin-down configuration, the main portion of the VB maxima is formed by the participation of the 3p/4p-states of S/Se. Aside from this, near E_F, a minor contribution can be seen by the 3d-states of Sc and Mn. Most of the CB minima is formed from contributions of the 3d–t$_{2g}$ and 3d–e$_g$ states of Mn and the 3d-states of Sc. However, very little is contributed by the 3p/4p states of S/Se.

3.4 Optical properties

For semiconductor materials, it is critical to understand their optical properties because of their role in the overall optoelectronic performance of such materials. In pursuit of this, the present study reports on the various optical parameters, which include the dielectric constant (ε), refractive index ($\tilde{n}$), absorption coefficient (α), and reflectivity (R), computed for both investigated materials. All the stated parameters were frequency-dependent and computed for the energy ranges from 0 to 10 eV. The first computed parameter is ε, which is associated with the decrease of the electromagnetic (EM) radiation in the material. It is a complex quantity and can be written as $\varepsilon(\omega) = \varepsilon_1(\omega) + i\varepsilon_2(\omega)$. The real part $\varepsilon_1(\omega)$ corresponds to the strength
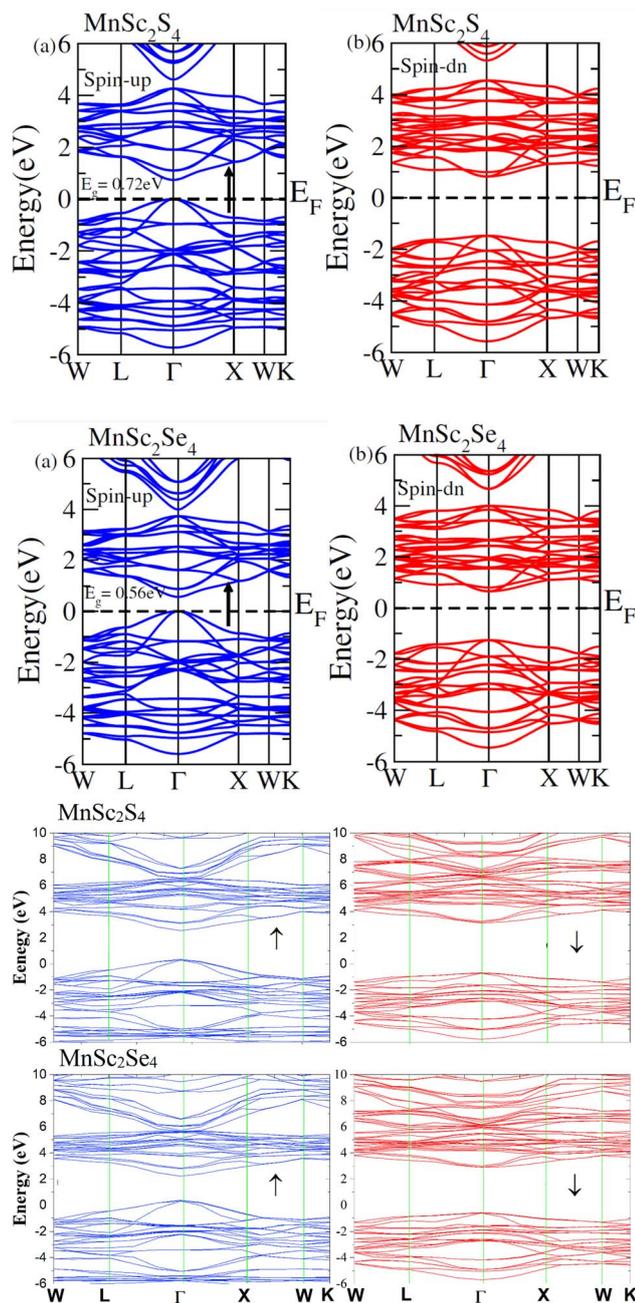
Fig. 4 (a) Electronic band structures for spinels $MnSc_2X_4$ (X = S, Se), computed with the mBJ potential. (b) Electronic band structures for spinels $MnSc_2X_4$ (X = S, Se), computed with HSE06.

of the polarization in the materials, and the imaginary part $\varepsilon_2(\omega)$ is associated with dielectric losses. Fig. 7(a) illustrates the computed plots of $\varepsilon_1(\omega)$, and revealed the value of static dielectric constant $\varepsilon_1(0)$ of 6.5 and 8.5 for $MnSc_2S_4$ and $MnSc_2Se_4$, respectively. The dielectric constant is related inversely with the bandgap such that $\varepsilon_1(0) \propto 1/E_g^2$.[34,35] Thus, there is a relatively greater magnitude of $\varepsilon_1(0)$ in the Se-based composition. Furthermore, at optical frequencies, $\varepsilon_1(\omega)$ decreases, which is due to the absence of dipolar polarization at those frequencies. In addition, $\varepsilon_1(\omega)$ has a positive magnitude

for both compositions throughout the frequency range. $\varepsilon_1(\omega)$ is related to the imaginary part $\varepsilon_2(\omega)$ through the Krammer–Koning's relations:[36]

$$\varepsilon_1(\omega) = 1 + \frac{2}{\pi} P \int_0^\infty \frac{\omega' \varepsilon_2(\omega')}{\omega'^2 - \omega^2} d\omega' \tag{8}$$

$\varepsilon_2(\omega)$ can be calculated by utilizing the following relation:

$$\varepsilon_2(\omega) = -\frac{2\omega}{\pi} P \int_0^\infty \frac{\varepsilon_1(\omega')}{\omega'^2 - \omega^2} d\omega' \tag{9}$$

Here, P is the Cauchy principal value. Fig. 7(b) presents the plots of $\varepsilon_2(\omega)$, which revealed that once the energy of the EM radiation exceeds the E_g values of both spin-configurations, the $\varepsilon_2(\omega)$ gives the steeper peaks. This can be explained in terms of losses due to the strong absorption at energies greater than E_g. The maximum magnitude of $\varepsilon_2(\omega)$ is obtained at 3.3 and 3.7 eV for $MnSc_2S_4$ and $MnSc_2Se_4$, respectively.

There is another complex optical parameter named the refractive index ($\tilde{n}$), which can be expressed as: $\tilde{n}(\omega) = n(\omega) + ik(\omega)$. The real part $n(\omega)$ equals the ratio of the speed of EM radiation in space to its speed in the medium. The imaginary part $k(\omega)$, also named the extinction coefficient, quantizes the loss of EM radiation per unit distance in the medium caused by absorption and scattering.[37] Fig. 7(c) and (d) illustrate the computed plots of $n(\omega)$ and $k(\omega)$, respectively. The magnitude of the real part of the refractive index for static field $n(0)$, as illustrated by the plots, is 2.75 and 2.9 for $MnSc_2S_4$ and $MnSc_2Se_4$, respectively. Its magnitude increases up to 2.5 eV, and then begins to decrease. Conversely, the plots of $k(\omega)$ give the peaks at the energy of 5.9 eV and 5.0 eV in the case of the S and Se-based compositions, respectively. The quantities $n(\omega)$ and $k(\omega)$ are linked with the dielectric constant by the relations: $\varepsilon_1 = n^2 + k^2$ and $\varepsilon_2 = 2nk$, respectively. Thus, $n(\omega)$ follows the same trend as that of $\varepsilon_1(\omega)$, and $k(\omega)$ shows a trend that is almost similar to $\varepsilon_2(\omega)$.

For semiconductors, the amount of light absorbed per unit distance in the material is very crucial to compute because the inter-band transition is associated with the absorption of light. To estimate this absorption, we compute the absorption coefficient (α), and its plots are illustrated in Fig. 7(e). The material only absorbs those photons of light having energy at least equal to the bandgap. It is apparent from the plots that once the energy of the EM radiation exceeds the bandgap value of both spin configurations, the absorption becomes stronger. Furthermore, the plots reveal that the two compositions exhibit strong absorption in the visible and ultraviolet (UV) regions of the spectra with most of the absorption in the UV region. For optoelectronic materials, the loss of EM radiation due to reflectance is important to note because it affects the device's performance. The reflectivity $R(\omega)$ for both materials was computed and is plotted in Fig. 7(f). The magnitude of $R(0)$ for $MnSc_2S_4$ and $MnSc_2Se_4$ is 0.22 and 0.24, which increases with the energy of the EM radiation, and has a maximum magnitude of 0.345 and 0.33, respectively, in the visible and near-UV regions.
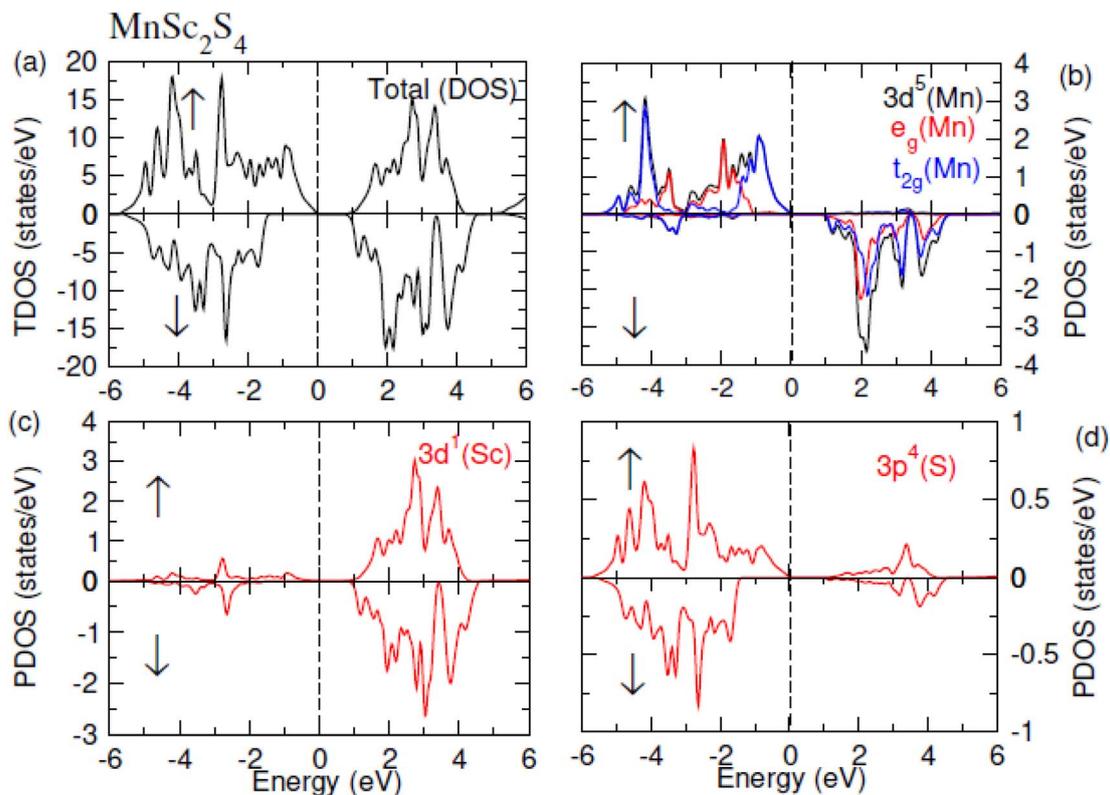
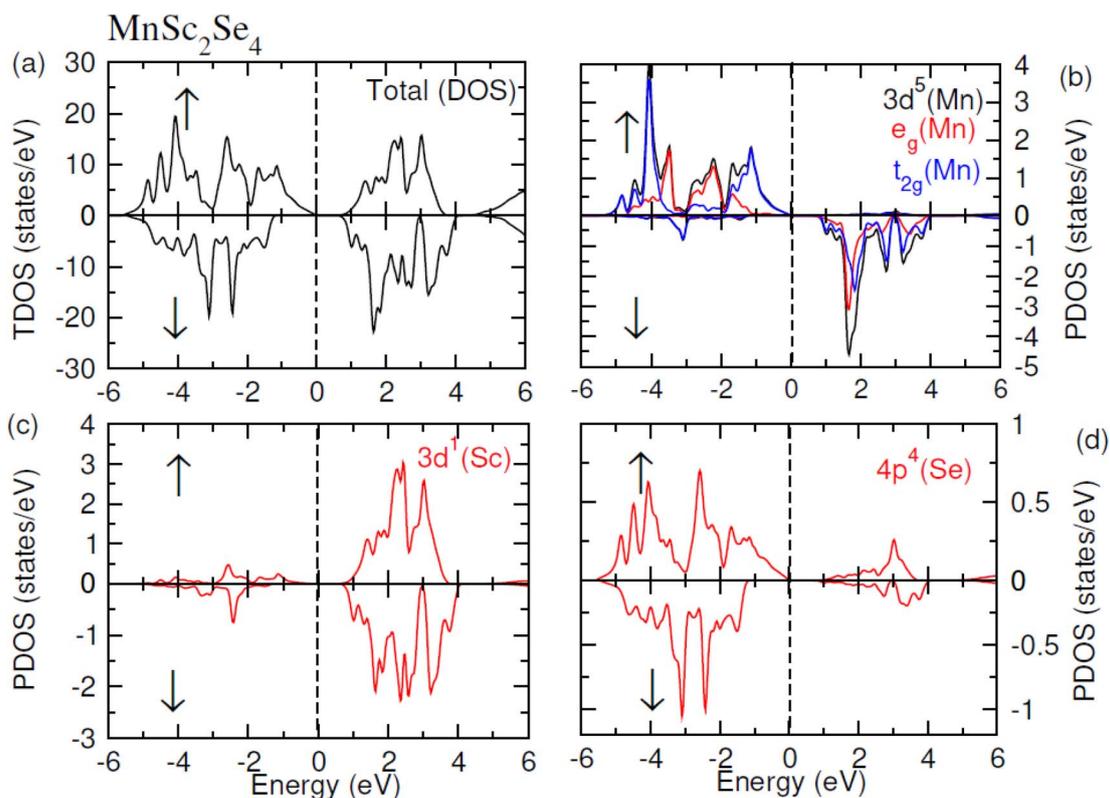**Fig. 5** (a) TDOS plot of MnSc2S4, PDOS plots of (b) Mn, (c) Sc and (d) S.

Fig. 6 (a) TDOS plot of MnSc2Se4, PDOS plots of (b) Mn, (c) Sc and (d) Se.
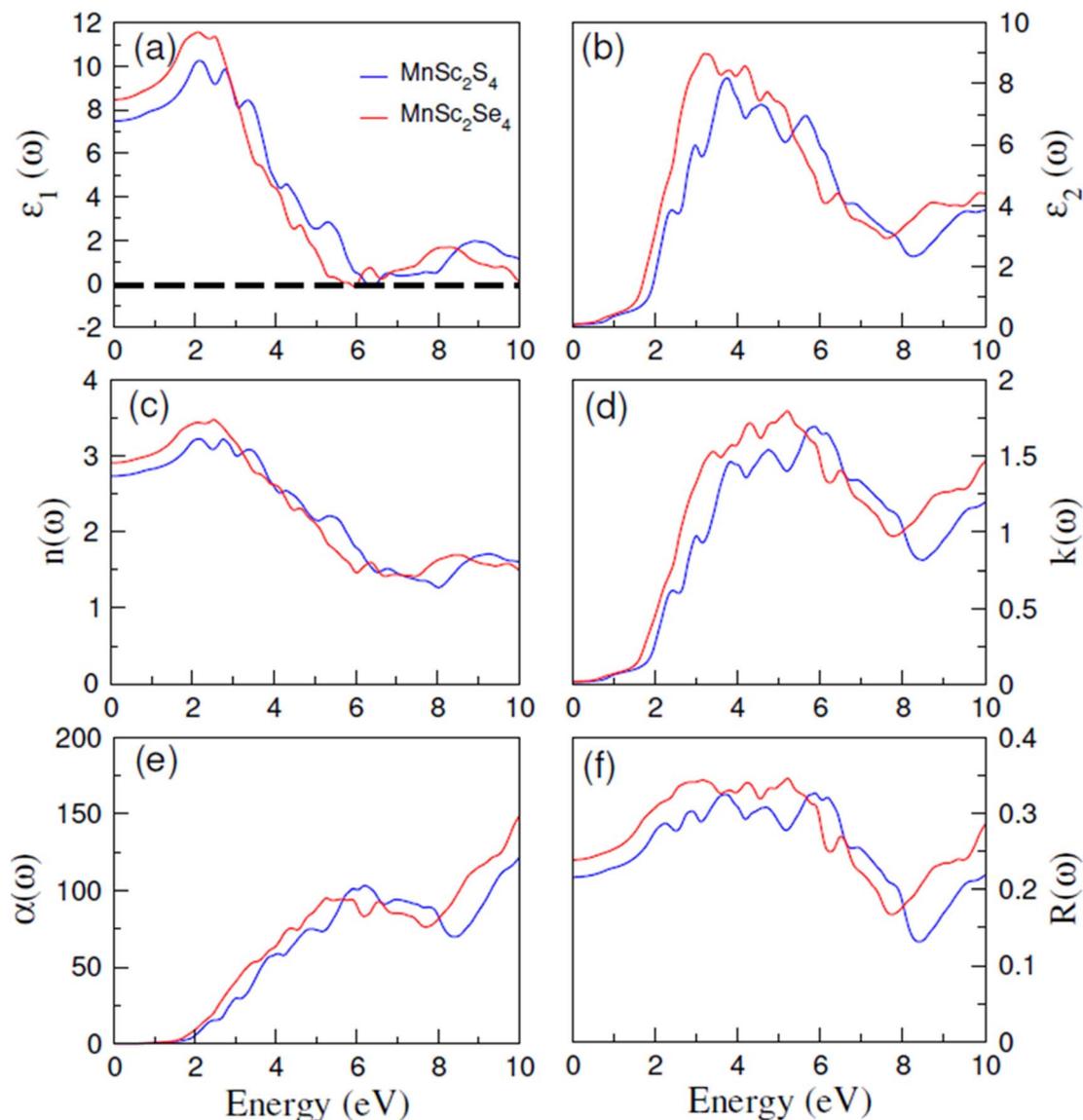
Fig. 7 Calculated values of (a) $\varepsilon_1(\omega)$, (b) $\varepsilon_2(\omega)$, (c) $n(\omega)$, (d) $k(\omega)$, (e) $\alpha(\omega)$, and (f) $R(\omega)$ for spinels $MnSc_2X_4$ (X = S, Se) in the energy range of 0 to 10 eV.

3.5 Magnetic properties

To analyze the magnetic behaviors observed in $MnSc_2S_4$ and $MnSc_2Se_4$, several key parameters have been thoroughly investigated, which include the exchange interactions, crystal field effects, and associated parameters. The observed variations in the bandgaps between the spin channels signify exchange splitting, resulting from the interactions between Mn and the anions (S or Se). The introduction of the S/Se atoms generates a crystal field, which splits the Mn 3d orbitals into five distinct energy levels. Among these, the nonlinear doublet e_g, comprising (d_{z^2}, $d_{x^2-y^2}$), experiences a greater energy increase compared to the linear triplet t_{2g}, which includes (d_{xy}, d_{yz}, d_{zx}). The bonding e_g states are energetically lower than the antibonding t_{2g} states, with the energy gap between them termed as the crystal field splitting energy (Δ_{CF}). Within the triplet states, the $d_{x^2-y^2}$ orbital has higher energy compared to the d_{yz} and d_{zx}.

orbitals, influencing the degeneracy patterns. This configuration aligns with Hund's rule, where unpaired electrons participate in hybridization. Such hybridization involves interactions between the Mn 3d orbitals and S/Se p orbitals, supporting the observed ferromagnetic behavior.

The energy band distribution shows that as a consequence of the exchange mechanism, the t_{2g} states migrate to reduced energies and the e_g states move to higher energies. Consequently, the lower-energy bonding states, which accommodate six 3d electrons of Mn, become occupied. A key parameter, the indirect exchange-splitting $\Delta_x(pd)$, is calculated by the location of the p-states of the anion within the down-spin configuration. Its value can be calculated using the Density of States (DOS) or band structure analysis, following the relation $\Delta(pd) = E_V^\downarrow - E_V^\uparrow$. A negative value for $\Delta(pd)$ signifies that the spin-down channel experiences stronger attraction compared to the spin-up channel. This behavior is a hallmark of spin-polarized

Table 2 Magnitude of anisotropy (A) in the computed elastic moduli (Y and G) and Poisson's ratios for MnSc$_2$X$_4$ (X = S, Se)

Parameters	Linear compressibility (β) (TPa^{-1})			Young's modulus (Y) (GPa)			Shear modulus (G) (GPa)			Poisson's ratio (ν)		
	β_{min}	β_{max}	A	Y_{min}	Y_{max}	A	G_{min}	G_{max}	A	ν_{min}	ν_{max}	A
MnSc$_2$S$_4$	244 230	244 230	1	0.0070567	0.01122	1.59	0.0055279	0.043178	7.811	−0.91057	−0.36172	0.3973
MnSc$_2$Se$_4$	197 150	197 150	1	0.007373	0.014479	1.964	0.0047678	0.099602	20.89	−0.98827	−0.22679	0.2295

materials, reflecting the asymmetry in energy levels due to spin-dependent interactions (Table 2).

The analysis sheds light on the magnetic properties of MnSc$_2$S$_4$ and MnSc$_2$Se$_4$ by incorporating the crystal field and exchange splitting, and the redistribution of electronic states, characterized by the Δ_{CF} for the up-spin and down-spin channels. Table 3 outlines the exchange splitting energy (Δ_xd), derived from the peak positions of the d-states in the down-spin ($\downarrow$) and up-spin ($\uparrow$) channels. The comparison between Δ_{CF} and Δ_xd reveals that Δ_xd is substantially greater compared to Δ_{CF}, highlighting the dominance of the ferromagnetic interactions over magnetic frustration in these compounds. This interplay between the exchange energies and crystal field effects underscores the mechanisms driving their magnetic behavior (Table 4).

The exchange interaction between the p orbitals of S/Se and the 3d orbitals of Mn generates exchange energy due to p–d coupling. The stabilization of ferromagnetism arises from the negative magnitude of the exchange energies, which reduce the overall energy of the system. The coupling of the conduction electrons and valence band holes with the d-orbitals of Mn is characterized by the s–d and p–d exchange constants depicted by $N_\circ\alpha$ and $N_\circ\beta$, respectively. The magnitude of these constants can be determined by the following expressions:

$$N_\circ\alpha = \frac{\Delta E_C}{x\langle S\rangle} \quad (10)$$

$$N_\circ\beta = \frac{\Delta E_V}{x\langle S\rangle} \quad (11)$$

Table 3 Estimated magnitudes of Δ_{CF}, $\Delta_x(d)$, $\Delta_x(pd)$, p–d and s–d exchange constants $N_\circ\beta$ and $N_\circ\alpha$, respectively, for MnSc$_2$S$_4$ and MnSc$_2$Se$_4$

Parameters	MnSc$_2$S$_4$	MnSc$_2$Se$_4$
Δ_{CF}	3.8	3.2
$\Delta_x(d)$	6.1	5.6
$\Delta_x(pd)$	−1.5	−1.2
$N_\circ\alpha$	0.12	0.07
$N_\circ\beta$	−0.72	−0.58

Table 4 Up-spin bandgap $\uparrow E_g$(eV), net, and the local magnetic moments (in Bohr magneton) computed for MnSc$_2$X$_4$ (X = S and Se)

	$\uparrow E_g$ (eV)	Total (μ_B)	Int. (μ_B)	Mn (μ_B)	Sc (μ_B)	X (μ_B)
MnSc$_2$S$_4$	0.72	5.0000	0.9700	4.1708	0.1209	0.0256
MnSc$_2$Se$_4$	0.56	5.0000	1.0041	4.1566	0.1254	0.0211

Here, (x) represents the degree of Mn participation, and $\langle S\rangle$ denotes the average magnetic moment. The negative magnitude of the indirect exchange energy at the edge of the valence band in the down-spin configuration reflects the system's energy minimization by means of double–exchange interaction. To further explore the ferromagnetic (FM) behavior, the splitting at the edges of the conduction band ($\Delta E_C = E_C^\downarrow - E_C^\uparrow$) and the edges of the valence band ($\Delta E_V = E_V^\downarrow - E_V^\uparrow$) is analyzed. These energy differences provide insights into the FM mechanism, with Table 3 summarizing the calculated exchange constants, which include both positive and negative values. In ferromagnetic systems, the negative exchange energy in the down-spin configuration plays a dominant role, consistent with the characteristics of indirect exchange interactions.

It is determined from the spin-dependent volume optimization that the investigated materials are FM in nature. However, the strength of the magnetization of the materials was evaluated by the measurement of their magnetic moment. The magnetic moment emerges due to the spin-polarized electrons, and it can be computed by the difference in the integral of spin-polarized DOS. In addition to the net magnetic moment, the local magnetic moment provided by individual ions in both compositions was computed and are listed in Table 3. Both compositions exhibit identical net magnetic moments with the magnitude of 5.000 μB, in which Mn alone contributes the magnetic moment of 4.1705 and 4.1566 μB in MnSc$_2$S$_4$ and MnSc$_2$Se$_4$, respectively. The reason for the high contribution of Mn is the unpaired electrons in its d-orbitals. This can also be visualized by the spin-polarized PDOS of the Mn ion, which shows the majority of the occupied up-spin states in the valence band. Aside from Mn, the contribution of Sc and S/Se is comparatively negligible. However, a decent portion of the magnetic moment comes from the interstitial region, which was also computed and tabulated in Table 3.

3.6 Thermoelectric properties

The major challenge with energy harvesting systems is their limited efficiency due to energy losses in the form of heat. In this regard, thermoelectric (TE) materials, capable of harvesting electrical energy from waste heat, are crucial to increase the efficiency of existing energy generation systems. In addition, these materials can be used as independent energy harvesting systems for sustainable energy solutions. Considering this, in the reported investigation, we computed the transport characteristics of MnSc$_2$S$_4$ and MnSc$_2$Se$_4$ using the BoltzTrap code. The reported transport parameters include the electrical and

thermal conductivities represented by σ and κ_e, respectively, and the Seebeck coefficient (S). All the mentioned parameters were computed against varying temperatures from 300 to 800 K. Since the spin-polarized nature of the materials leads to different magnitudes of the computed parameters in different spin orientation, the following equations were used to compute the net magnitude of these parameters.[38]

$$\sigma = \frac{\sigma^\uparrow + \sigma^\downarrow}{2} \qquad (12)$$

$$\kappa_e = \frac{\kappa_e^\uparrow + \kappa_e^\downarrow}{2} \qquad (13)$$

$$S = \frac{\sigma^\uparrow S^\uparrow + \sigma^\downarrow S^\downarrow}{\sigma^\uparrow + \sigma^\downarrow} \qquad (14)$$

Fig. 8(a) illustrates the computed plots of σ/τ, which revealed that its magnitude increases almost linearly with temperature. The semiconducting nature of the composition accounts for this increasing trend. The increasing temperature supplies thermal energy to the materials, enough to excite the electrons to the conduction band and hence increase the carrier concentration, which in turn increases the electrical conductivity. At 300 K, the computed magnitude of σ/τ is 0.066×10^{19} $(\Omega\text{ ms})^{-1}$ and 0.07×10^{19} $(\Omega\text{ ms})^{-1}$, which increases and reaches its maximum at 800 K with the magnitude of 0.307×10^{19} $(\Omega\text{ ms})^{-1}$ and 0.278×10^{19} $(\Omega\text{ ms})^{-1}$ for $MnSc_2S_4$ and $MnSc_2Se_4$, respectively. In regards to thermal conductivity, it comprises two components: $\kappa = \kappa_e + \kappa_L$; where, κ_e represents the part that is contributed by the charge carriers, and κ_L signifies the part that comes from the lattice vibrations. The κ_e/τ was computed using
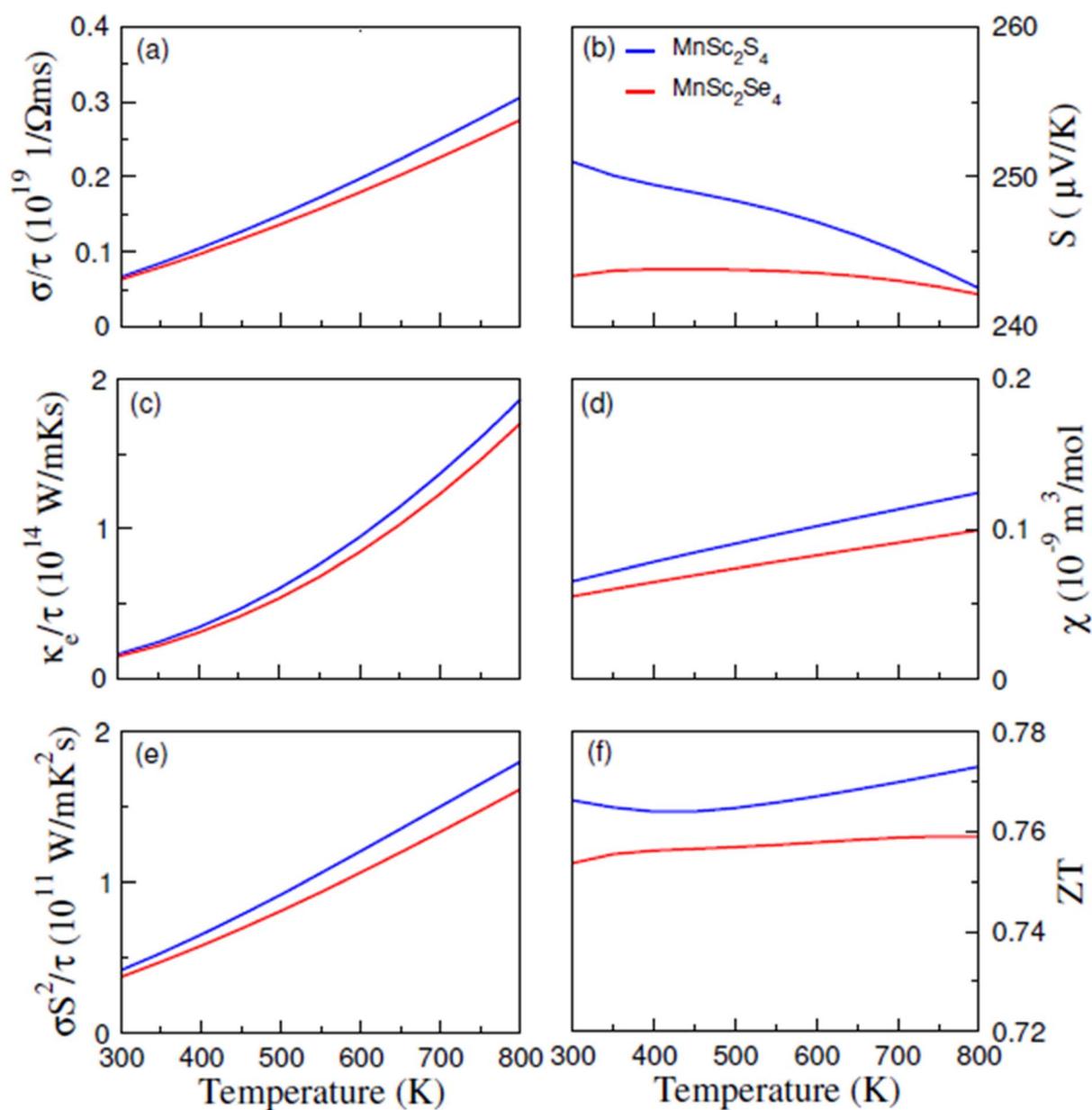

Fig. 8 Estimated plots of (a) σ/τ, (b) S, (c) k_e/τ, (d) χ, (e) P.F. and (f) ZT against increasing temperatures for spinel compounds $MnSc_2X_4$ (X = S, Se).
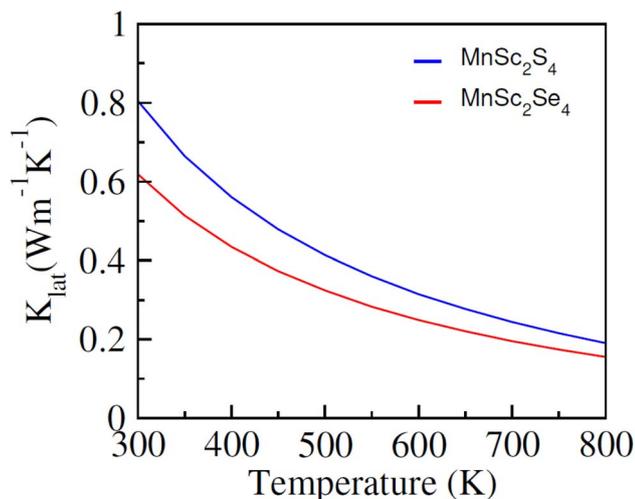
Fig. 9 Computed lattice conductivity (k_{lat}) for spinel compounds MnSc$_2$X$_4$ (X = S, Se) against temperature.

the BoltzTrap code and its plots are elucidated in Fig. 8(c), which show a roughly similar increasing trend as with σ/τ. At 300 K, the magnitude of κ_e/τ is 0.17×10^{14} W mK^{-1} s^{-1} for both MnSc$_2$S$_4$ and MnSc$_2$Se$_4$, which reaches its maximum value of 1.87×10^{14} and 1.7×10^{14} W mK^{-1} s^{-1} at 800 K, respectively. Moreover, the lattice part of the thermal conductivity (κ_L) has been investigated by employing ShengBTE code,[39] as illustrated in Fig. 9. The magnitudes of κ_L for MnSc$_2$S$_4$ and MnSc$_2$Se$_4$ gradually decrease from 0.80 and 0.61, respectively, when the temperature increases from 200 to 800 K. The magnitudes of κ_L are particularly inferior to κ_e, indicating that the thermoelectric efficiency is not decisively affected by the κ_L of MnSc$_2$S$_4$ and MnSc$_2$Se$_4$. Thus, the performance analysis factor ZT is slightly altered by κ_L.

When a TE material is exposed to a temperature gradient, then a voltage is generated across its terminals quantified by the Seebeck coefficient (S). The parameters that influence the magnitude of S are given in the following equation:[40]

$$S = \frac{8\pi^2 k_B}{3eh^2} m^* T \left(\frac{\pi}{3n}\right)^{\frac{2}{3}} \quad (15)$$

In this relation, k_B, h, and e are constant quantities and represent the Boltzmann constant, Planck's constant, and charge on the charge carrier. T, m^* and n denote the absolute temperature, carrier's effective mass and carrier concentration, respectively.

Fig. 8(b) depicts the plots of S, computed for MnSc$_2$S$_4$ and MnSc$_2$Se$_4$. Both compositions have a good value of S, which is greater than 240 μV K^{-1}, for the whole temperature range. Furthermore, the positive values of S signify the p-type nature of the materials. For MnSc$_2$S$_4$, the graph shows the magnitude of 251 μV K^{-1} at 300 K, which decreases non-linearly and becomes 242.5 μV K^{-1} at 800 K. The increase in the carrier concentration (n) caused by the increasing temperature is the reason for this decrease in S. In the case of MnSc$_2$Se$_4$, the magnitude of S at 200 K is 243 μV K^{-1}, which has a negligible net change with temperature, and becomes 242 μV K^{-1} at the temperature of 800 K. It seems that the decrease in the value of S due to the increasing carrier concentration is neutralized with the increase in its magnitude due to temperature.

Since, the materials showed magnetic behavior, their ability to be magnetized when exposed to an external magnetic field can be analyzed by the parameter called magnetic susceptibility (χ). The variation in χ against the increasing temperature was computed, and is illustrated in Fig. 8(d). The plots demonstrate that both compositions have nearly identical linear increases in the χ with temperature. At 800 K, the maximum values of the χ for S and Se-based composition are 0.125×10^{-9} and 0.1×10^{-9} m^3 mol^{-1}, respectively. We assess the efficiency of the materials in harvesting energy from heat using a parameter known as the power factor (P.F. = $\sigma S^2/\tau$). Fig. 8(e) presents the plots of the computed P.F., which unveil the increasing trend with temperature. This increasing trend comes from the increased
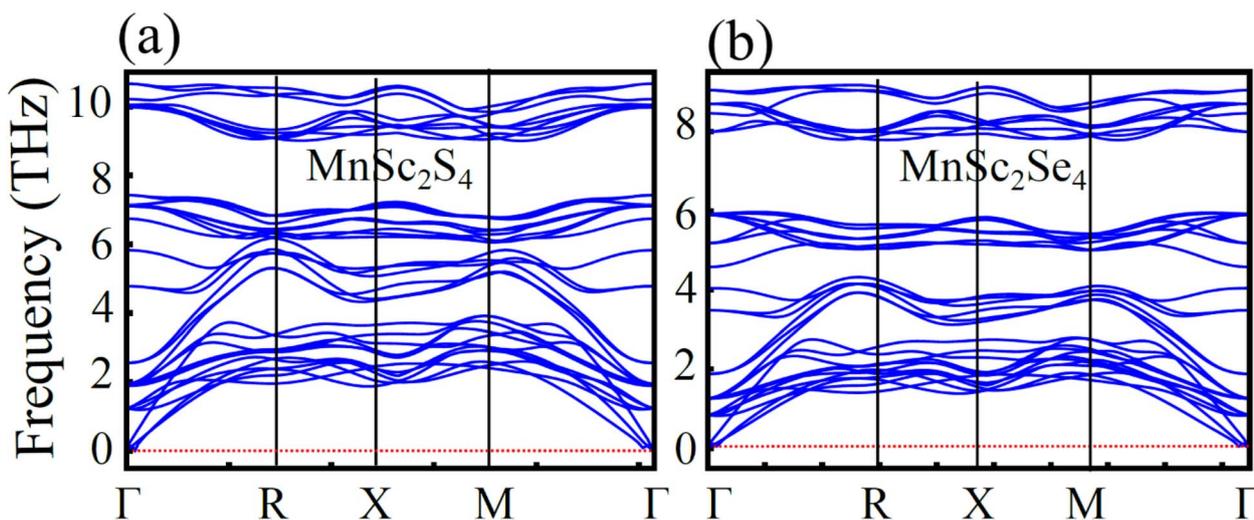

Fig. 10 Phonon dispersion for spinel compounds (a) MnSc$_2$S$_4$ and (b) MnSc$_2$Se$_4$.

electrical conductivity at high temperatures. For $MnSc_2S_4$ and $MnSc_2Se_4$, the magnitude of P.F at 300 K is 0.4×10^{11} and 0.35×10^{11} W mK^{-2} s^{-1}, which increases and reaches its maximum at 800 K with the value of 1.8×10^{11} and 1.64×10^{11} W mK^{-2} s^{-1}, respectively. At the end, the overall TE functionality of the investigated spinels was probed through the dimensionless variable named the figure of merit (ZT), which is calculated by using the previously computed parameters, such that $ZT = (S^2\sigma/\kappa_e)T$. The plots in Fig. 8(f) depict a high ZT value of 0.76 to 0.77 with a negligible variation throughout the temperature range, making the material equally effective for room and high-temperature TE applications.

3.7 Phonon dispersion plot

To probe the dynamic stability, calculations of the phonon dispersion along the high-symmetry point within the Brillouin zone were performed, and the phonon dispersion curves are plotted in Fig. 10. The plot demonstrates that all of the vibrational modes are positive in the Brillouin zone for $MnSc_2S_4$ and $MnSc_2Se_4$, which is an indication of the compounds' dynamic stability. On the other hand, the existence of negative frequencies is indicator of instability in some forms of the vibrational states, but no such frequency is depicted in the computed plots.

4.   Conclusion

A detailed investigation of the mechanical, optoelectronic, and magnetic properties of the chalcogenide spinels $MnSc_2X_4$ (X = S, Se) was conducted by employing the density functional theory. The spinels were observed to have cubic structures with the $Fd\bar{3}m$ space group. The mechanical stability of the spinels was validated by the calculated magnitudes of elastic stiffness constants. Furthermore, their ductile nature was attested by the computed Poisson's and Pugh's ratios, which exhibited magnitudes greater than 0.26 and 1.75, respectively. The thermodynamic stability was assessed by the formation energies (ΔH_f), which were −1.45 and −1.34 eV in the case of $MnSc_2S_4$ and $MnSc_2Se_4$ respectively. The negative magnitude revealed that formation involves an exothermic reaction, which confirmed the thermodynamic stability. Furthermore, the S-based composition had a greater magnitude of ΔH_f, which made it relatively more stable. The spin-polarized EBS and DOS demonstrated the semiconducting behavior with the direct bandgap of 0.72 and 0.56 eV in the spin-up orientation for $MnSc_2S_4$ and $MnSc_2S_4$, respectively. Furthermore, the materials exhibited high absorption in the visible to UV region of the spectrum, making them suitable for solar cells and UV-detection applications. In terms of their magnetic characteristics, the materials exhibit a ferromagnetic nature with a magnetic moment of 5.000 μB, which was primarily attributed to the Mn ions. The thermoelectric characteristics were also analyzed by BoltzTrap code, which revealed the high Seebeck coefficient in the range of 242 to 251 μV K^{-1} for the temperature range of 300 to 800 K. With increasing electrical conductivity and a decent figure of merit, the materials show potential for thermoelectric applications. Overall, the outcomes of the study demonstrate that the materials are suitable for optoelectronic and thermoelectric applications.

Data availability

All data included in this research will be made available upon request.

Conflicts of interest

There is no conflict to declare.

Acknowledgements

References

1 F. Adams and C. Barbante, Nanotechnology and analytical chemistry, *Compr. Anal. Chem.*, 2015, **69**, 125–157.

2 T. Y. Lee, L. Y. Chen, Y. Y. Lo, S. S. Swayamprabha, A. Kumar, Y. M. Huang and H. C. Kuo, Technology and applications of micro-LEDs: their characteristics, fabrication, advancement, and challenges, *ACS Photonics*, 2022, **9**(9), 2905–2930.

3 D. Decoster and J. Harari, *Optoelectronic Sensors*, John Wiley & Sons, 2013.

4 Z. Chen, S. N. Obaid and L. Lu, Recent advances in organic optoelectronic devices for biomedical applications, *Opt. Mater. Express*, 2019, **9**(9), 3843–3856.

5 U. L. Osterberg, Optical fiber, cables, and connectors, in *Handbook of Fiber Optic Data Communication*, Academic Press, 2008, pp. 19–42.

6 M. U. Sohaib, K. Abid, N. A. Noor, M. A. Khan, R. Neffati, S. H. Abdel-Hafez and E. E. Hussein, Comprehensive DFT investigation of Cd-based spinel chalcogenides for spintronic and solar cells devices, *J. Mater. Res. Technol.*, 2021, **15**, 4683–4693.

7 Y. D. Tretyakov, I. V. Gordeev and Y. A. Kesler, Investigation of some chalcogenides with spinel structure, *J. Solid State Chem.*, 1977, **20**(4), 345–358.

8 A. Satpathy, W. T. Huang, T. H. Liu, T. Y. Su, W. Zhang, M. Kamiński and R. S. Liu, Mini light-emitting diode technology with high quantum efficient NIR-II partially inverse spinel $MgGa_2O_4$: Cr^{3+}, Ni^{2+} nanophosphors, *Adv. Opt. Mater.*, 2024, **12**(19), 2400130.

9 V. Jagadeesha Angadi, K. Manjunatha, M. C. Oliveira, E. Longo, S. R. de Lázaro, R. A. P. Ribeiro and S. V. Bhat, Unveiling the shape-selective $CoCr_2-yScyO_4$ nanomagnetism, *Appl. Surf. Sci.*, 2022, **574**, 151555.

10 V. Tsurkan, H. A. K. von Nidda, J. Deisenhofer, P. Lunkenheimer and A. Loidl, On the complexity of spinels: magnetic, electronic, and polar ground states, *Phys. Rep.*, 2021, **926**, 1–86.

11 K. Manjunatha, V. J. Angadi, R. A. P. Ribeiro, E. Longo, M. C. Oliveira, M. R. D. Bomio, S. R. d. Lazaro,

S. Matteppanavar, S. Rayaprol, P. D. Babu and M. Pasha, Structural, electronic, vibrational and magnetic properties of Zn^{2+} substituted $MnCr_2O_4$ nanoparticles, *J. Magn. Magn. Mater.*, 2020, **502**, 166595.

12 K. Manjunatha, H. H. Chiu, M. K. Ho, T. E. Hsu, S. L. Yu, C. E. Chin, C. L. Cheng, M. C. De Oliveria, E. Logo, R. A. Ribeiro and H. Nagabhushana, Mg-doped $CoCr_2O_4$ nanoparticles: implications for magnetic memory and magnetocaloric effect, *ACS Appl. Nano Mater.*, 2023, **6**, 12002–12015.

13 P. Sánchez-Palencia, G. García, J. C. Conesa, P. Wahnón and P. Palacios, Spinel-type nitride compounds with improved features as solar cell absorbers, *Acta Mater.*, 2020, **197**, 316–329.

14 A. Zerr, R. Riedel, T. Sekine, J. E. Lowther, W. Y. Ching and I. Tanaka, Recent advances in new hard high-pressure nitrides, *Adv. Mater.*, 2006, **18**(22), 2933–2948.

15 F. Di Quarto, A. Zaffora, F. Di Franco and M. Santamaria, Modeling of optical band-gap values of mixed oxides having spinel structure AB_2O_4 (A= Mg, Zn and B= Al, Ga) by a semiempirical approach, *ACS Org. Inorg. Au*, 2023, **4**(1), 120–134.

16 A. Jouini, A. Yoshikawa, A. Brenier, T. Fukuda and G. Boulon, Optical properties of transition metal ion-doped $MgAl_2O_4$ spinel for laser application, *Phys. Status Solidi C*, 2007, **4**(3), 1380–1383.

17 G. J. Snyder, T. Caillat and J. P. Fleurial, Thermoelectric properties of chalcogenides with the spinel structure, *Mater. Res. Innovations*, 2001, **5**, 67–73.

18 N. A. Noor, F. Nasrullah, I. M. Moussa and S. Mumtaz, Mechanical, magnetic, and electronic characteristics of Sm-based chalcogenides for spintronics and device applications, *Chalcogenide Lett.*, 2024, **21**(5), 413–421.

19 G. M. Mustafa, S. Saba, N. A. Noor, A. Laref, M. Abd El-Rahman, Z. Farooq and Z. Ullah, First-principles calculations to investigate HgY_2S/Se_4 spinel chalcogenides for optoelectronic and thermoelectric applications, *J. Mater. Res. Technol.*, 2023, **22**, 97–106.

20 F. Shahid, B. Ismail, A. M. Khan, Q. U. Ain, R. A. Khan, F. Shah, T. Fazal and M. N. Asghar, Cost effective way of tuning physical properties of $MgAl_2O_4$ spinel nanomaterials by Sr^{+2}/Mn^{2+} cations doped at the T-sites, *Ceram. Int.*, 2020, **46**(8), 10710–10717.

21 W. Tahir, G. M. Mustafa, N. A. Noor, S. M. Alay-e-Abbas, Q. Mahmood and A. Laref, Analysis of optoelectronic and transport properties of magnesium-based $MgSc_2X_4$ (X = S, Se) spinels for solar cell and energy storage device applications, *Ceram. Int.*, 2020, **46**(17), 26637–26645.

22 M. Sameeullah, M. Ishfaq, S. A. Aldaghfag, M. Yaseen, M. Nazar and A. Dahshan, Magnetic, optoelectronic, and thermoelectric characteristics of Ln_2MnSe_4 (Ln = Yb, Lu) spinel chalcogenides: a DFT investigation, *J. Solid State Chem.*, 2023, **326**, 124238.

23 F. Tran and P. Blaha, Accurate band gaps of semiconductors and insulators with a semilocal exchange-correlation potential, *Phys. Rev. Lett.*, 2009, **102**(22), 226401.

24 H. Albalawi, A. Azazi, Q. Mahmood, N. A. Kattan, S. Al-Qaisi, G. Murtaza, F. Ercan, S. Bouzgarrou and M. Jadan, Study of role of spin in ferromagnetism and thermoelectric characteristics of spinel chalcogenides $MgEr_2(S/Se)_4$ for spintronic and clean energy, *J. Solid State Chem.*, 2023, **324**, 124128.

25 F. Mouhat and F. X. Coudert, Necessary and sufficient elastic stability conditions in various crystal systems, *Phys. Rev. B*, 2014, **90**(22), 224104.

26 G. M. Mustafa, B. Younas, M. Waseem, N. A. Noor, K. M. Elhindi and S. Mumtaz, Investigation of optoelectronic and thermoelectric characteristics of Tl_2Os (Cl/Br) 6 double perovskites for renewable energy applications, *Mater. Sci. Semicond. Process.*, 2025, **192**, 109420.

27 L. Dong, S. Sun, Z. Deng, W. Li, F. Wei, Y. Qi, Y. Li, X. Li, P. Lu and U. Ramamurty, Elastic properties and thermal expansion of lead-free halide double perovskite $Cs_2AgBiBr_6$, *Comput. Mater. Sci.*, 2018, **141**, 49–58.

28 H. H. Hegazy, G. M. Mustafa, A. Nawaz, N. A. Noor, A. Dahshan and I. Boukhris, Tuning of direct bandgap of Rb_2ScTlX_6 (X = Cl, Br, I) double perovskites through halide ion substitution for solar cell devices, *J. Mater. Res. Technol.*, 2022, **19**, 1271–1281.

29 Q. Long, X. Nie, S. L. Shang, J. Wang, Y. Du, Z. Jin and Z. K. Liu, $C_{15}NbCr_2$ Laves phase with mechanical properties beyond Pugh's criterion, *Comput. Mater. Sci.*, 2016, **121**, 167–173.

30 D. H. Wu, H. C. Wang, L. T. Wei, R. K. Pan and B. Y. Tang, First-principles study of structural stability and elastic properties of $MgPd_3$ and its hydride, *J. Magnesium Alloys*, 2014, **2**(2), 165–174.

31 I. E. Castelli, J. M. García-Lastra, K. S. Thygesen and K. W. Jacobsen, Bandgap calculations and trends of organometal halide perovskites, *APL Mater.*, 2014, **2**(8), 081514.

32 S. X. Tao, X. Cao and P. A. Bobbert, Accurate and efficient band gap predictions of metal halide perovskites using the DFT-1/2 method: GW accuracy with DFT expense, *Sci. Rep.*, 2017, **7**(1), 14386.

33 Q. Mahmood, G. M. Mustafa, N. A. Kattan, T. Alshahrani, N. Sfina, A. Mera, Z. H. Shah, H. H. Somaily, S. Alharthi and M. A. Amin, Tuning of band gap of double perovskite halides Rb_2CuSbX_6 (X = Cl, Br, I) for solar cells and energy harvesting, *Mater. Sci. Eng., B*, 2022, **286**, 116088.

34 R. Ravichandran, A. X. Wang and J. F. Wager, Solid state dielectric screening *versus* band gap trends and implications, *Opt. Mater.*, 2016, **60**, 181–187.

35 Y. Dong, R. Zhu and Y. Jia, Linear relationship between the dielectric constant and band gap in low-dimensional mixed-halide perovskites, *J. Phys. Chem. C*, 2021, **125**(27), 14883–14890.

36 R. Lovell, Application of Kramers-Kronig relations to the interpretation of dielectric data, *J. Phys. C: Solid State Phys.*, 1974, **7**(23), 4378.

37 N. A. Bakr, A. M. Funde, V. S. Waman, M. M. Kamble, R. R. Hawaldar, D. P. Amalnerkar, S. W. Gosavi and

S. R. Jadkar, Determination of the optical parameters of a-Si:H thin films deposited by hot wire–chemical vapour deposition technique using transmission spectrum only, *Pramana*, 2011, **76**, 519–531.

38 G. A. Mersal, H. Alkhaldi, G. M. Mustafa, Q. Mahmood, A. Mera, S. Bouzgarrou, A. Badawi, A. A. Shaltout, J. Boman and M. A. Amin, Study of half metallic ferromagnetism and thermoelectric properties of spinel chalcogenides $BaCr_2X_4$ (X = S, Se, Te) for spintronic and energy harvesting, *J. Mater. Res. Technol.*, 2022, **18**, 2831–2841.

39 W. Li, J. Carrete, N. A. Katcho and N. Mingo, ShengBTE: A solver of the Boltzmann transport equation for phonons, *Comput. Phys. Commun.*, 2014, **185**(6), 1747–1758.

40 N. H. Alotaibi, G. M. Mustafa, N. A. Kattan, Q. Mahmood, H. Albalawi, M. Morsi and M. A. Amin, DFT study of double perovskites Cs_2AgBiX_6 (X = Cl, Br): an alternative of hybrid perovskites, *J. Solid State Chem.*, 2022, **313**, 123353.